# CFD Validation of Small Quadrotor Performance using CREATE<sup>TM</sup>-AV Helios

# Austin D. Thai **Graduate Student Boston University** Boston, MA

# **Rohit Jain**

Aerospace Engineer Aviation Development Directorate U.S. Army Combat Capabilities

Development Command Aviation & Missile Center Ames Research Center, Moffett Field, CA

# Sheryl M. Grace Associate Professor **Boston University** Boston, MA

## **ABSTRACT**

Computational fluid dynamics (CFD) simulations of a small quadrotor were conducted using CREATE<sup>TM</sup>-AV Helios. Two near-body CFD solvers and multiple turbulence models including transition models available in Helios were tested. The DJI Phantom 3 was chosen as a representative configuration because it has been studied extensively and is typical of commercial unmanned aerial vehicles. The airfoil at three-quarters span of the rotor geometry was extracted to perform both two-dimensional (2D) airfoil and three-dimensional (3D) wing studies in order to determine appropriate grid spacings for use with the various models. Isolated rotor simulations for DJI Phantom 3 rotor in hover utilizing appropriate grids were completed for fully turbulent and turbulence transition models. The predicted thrust from all of the methods lie within experimental uncertainty. The Spalart Allmaras model gave consistent results across the two CFD solvers and was most computationally efficient. As such it was chosen for the simulations of the full quadrotor performance in hover. The results indicate that a transition model is not required in order to obtain satisfactory thrust predictions as compared to experiment for a small quadrotor in hover using the Helios package. However, the figure of merit is underpredicted by both fully turbulent and transition models. Therefore, the effect of transition modeling on torque prediction needs further investigation.

## **ABBREVIATIONS**

# **NOTATION**

CFD	Computational Fluid Dynamics	c
2D	Two-dimensional	R
3D	Three-dimensional	S
RANS	Reynolds-Averaged Navier-Stokes	Γ
UAV	Unmanned Aerial Vehicle	Q
NASA	National Aeronautics and Space Administration	$\tilde{f}_{thresho}$
DELIVER	Design Environment for Novel Vertical Lift	$y^+$
	Vehicles	η
UTM	UAS Traffic Management	$\dot{C}_T$
RVLT	Revolutionary Vertical Lift Technology	$C_Q$
SA	Spalart-Allmaras	$T^{\sim}$
k-ω	k-omega Shear Stress Transport	M
LM	Langtry-Menter	Ω
AFT	Amplification Factor Transport	$\boldsymbol{A}$
MB	Medida-Baeder	ρ
M15	Menter 2015	,
DoD	Department of Defense	
HPC	High performance computing	
CAD	Computer Aided Design	There is
AMR	Adaptive Mesh Refinement	ulation of
DES	Detached Eddy Simulation	type of
LES	Large Eddy Simulation	nonulari
	2D 3D RANS UAV NASA DELIVER  UTM RVLT SA k-ω LM AFT MB M15 DoD HPC CAD AMR DES	2D Two-dimensional 3D Three-dimensional RANS Reynolds-Averaged Navier-Stokes UAV Unmanned Aerial Vehicle NASA National Aeronautics and Space Administration DELIVER Design Environment for Novel Vertical Lift Vehicles UTM UAS Traffic Management RVLT Revolutionary Vertical Lift Technology SA Spalart-Allmaras k-\omega Shear Stress Transport LM Langtry-Menter AFT Amplification Factor Transport MB Medida-Baeder M15 Menter 2015 DoD Department of Defense HPC High performance computing CAD Computer Aided Design AMR Adaptive Mesh Refinement DES Detached Eddy Simulation

Presented at the Vertical Flight Society 75th Annual Forum & Technology Display, Philadelphia, Pennsylvania, May 13-16, 2019. This material is declared a work of the U.S. Government and is not subject to copyright protection in the United States. DISTRIBUTION STATEMENT A: Approved for public release; distribution is unlim-

c	chord length, m
R	rotor radius, m
S	strain rate tensor, $s^{-1}$
Γ	rotation rate tensor, $s^{-1}$
Q	Q-criterion, $s^{-1}$
$f_{threshold}$	adaptation threshold function
$y^+$	dimensionless wall distance
η	figure of merit
$C_T$	thrust coefficient
$C_Q$	torque coefficient
$\tilde{T}$	thrust, N
M	moment about the rotor axis, $N - m$
Ω	rotor rotation speed, <i>rad/s</i>
$\boldsymbol{A}$	rotor area, $m^2$
ρ	air density, $kg/m^3$

#### INTRODUCTION

is a growing demand for accurate high-fidelity simof aerodynamic performance of small quadrotors, a unmanned aerial vehicle (UAV), due to increased popularity of these devices for military and civilian applications. Flow solvers for rotorcraft have typically been developed for helicopters, whose Reynolds numbers typically operate in the turbulent flow regime. Fully turbulent flows are commonly modeled using Reynolds-Averaged Navier-Stokes (RANS) equations with a turbulence model for closure of the



Fig. 1: DJI Phantom 3 (Ref. 1).

Reynolds stresses. However, small quadrotor aerodynamics operate in the turbulence-transition regime, and therefore pose a challenge to computational fluid dynamics (CFD). In this paper, a software package developed for simulation of large rotorcraft, CREATE<sup>TM</sup>-AV Helios, is tested for its ability to simulate performance of a small quadrotor.

It was surmised that turbulence-transition models not utilized for the large rotorcraft simulations would be important for the simulation of smaller vehicles. Therefore, effort was spent testing the available transition models on simpler, relevant, geometries such as a single airfoil and a straight wing. Lessons concerning appropriate grids for use with the available transition models were then used to perform a validation study focused on the isolated rotor case. Both accuracy and required computational resources are then used as a metric to determine a turbulence model to be used for the full quadrotor simulations.

Of particular interest is the assessment of two different solvers that include turbulence transition models available in Helios. Both NASA FUN3D, a finite-volume unstructured-grid solver, and mStrand, a finite-volume strand grid solver, are studied.

This paper demonstrates the strengths of these computational approaches by comparing aerodynamic performance results with experimental data for the DJI Phantom 3 with 9450 rotor blades. A picture of the DJI Phantom 3 can be seen in Fig. 1. After a discussion of prior work, the experimental work conducted at NASA Ames Research Center is outlined. Then, the computational methodology is described. Computational studies of the different turbulence models are conducted for an airfoil and a wing. A grid convergence study is performed for download on a bare fuselage so that the appropriate grid is used in the quadrotor studies. Finally, both the isolated rotor simulations and the full quadrotor simulations, consisting of the fuselage and all four rotors, is presented. The predicted thrust results for the isolated rotor and the full quadrotor are validated with experimental values.

## **BACKGROUND**

Computational simulations of small quadrotors have been presented previously. However, these studies lack detailed validation. Hwang et al. (Ref. 2) used a 3D, incompressible, RANS unstructured solver with overset mesh capability to show that a diamond configuration quadrotor with one fore and one aft rotor increased the overall lift capacity of the vehicle. Misiorowski et al. (Ref. 3) was recently able to replicate these results using a finite element commercial solver Acu-Solve to study the effect of rotor configuration on forward flight. Yoon et al. and Diaz et al. (Refs. 4, 5) used NASA's structured-mesh grid solver OVERFLOW to model multirotor UAVs and showed thrust improvements with hybrid configurations of rotor placement as well. Christian et al. (Ref. 6) and Zawodny et al. (Ref. 7) both used OVERFLOW to perform isolated rotor calculations, showing good agreement with experiments and subsequently used these results to make successful acoustic trend predictions. The previous single rotor and quadrotor computations have all utilized simplified propeller geometries, in which the hubs were removed or separated from the blades, and thus could not validate the predictions against experimental measurements.



Fig. 2: Fuselage geometry.



Fig. 3: Rotor geometry.

In this work, the actual DJI geometry, as shown in Figs. 2 & 3 will be simulated via CREATE<sup>TM</sup>-AV Helios. To verify the results, the thrust and figure of merit will be compared to experimental data. OVERFLOW has been used extensively to study quadrotors, so this work seeks to extend the literature by using FUN3D and mStrand. Both are available as near-body solvers in CREATE<sup>TM</sup>-AV Helios. Previously, unstructured grid solvers, including Helios with FUN3D, have successfully implemented turbulence transition models for simulating helicopters in hover (Refs. 8–12). The Helios suite with mStrand as the solver has also been validated for many different types of complex flows, involving both fixed wing aircraft and rotorcraft, demonstrating robustness and accuracy (Refs. 13–15).

#### EXPERIMENTAL WORK

Performance data for the DJI Phantom 3 with plastic 9450 rotors in hover and in forward flight were obtained by researchers at NASA Ames as part of three different projects: the Design Environment for Novel Vertical Lift Vehicles (DELIVER) project, the UAS Traffic Management (UTM) project, and the Revolutionary Vertical Lift Technology (RVLT) project (Refs. 16,17). Specifications for the DJI Phantom 3 can be found in Table 1. Both isolated rotor and full quadrotor configurations were tested at multiple flight attitudes and RPMs. Forces and moments were measured using a six-axis load cell manufactured by JR3 Inc. Drag and lift on the bare airframe of the vehicle's fuselage were also measured at different wind speeds and pitch angles. The hover data for both the single rotor and full configuration which are of interest for validation of the current simulations were collected in a large lab space.

Table 1: DJI Phantom 3 characteristics.

Characteristic	English	Metric
Weight (no payload)	2.82 lbs	1.28 kg
Rotor Diameter	9.44 in	240 mm
Average Chord Length	1 in	2.54 mm
Tip Chord Length	0.429 in	10.9 mm
Operating RPM	2500	- 8000
Tip Mach Number	0.091	- 0.293
Tip Reynolds Number	41,500 -	133,000

# **COMPUTATIONAL METHODOLOGY**

#### CREATE<sup>TM</sup>-AV Helios

Helios is a high-fidelity, multidisciplinary rotorcraft modeling software developed under the sponsorship from High Performance Computing Modernization Program Computational Research and Engineering Acquisition Tools and Environments Air Vehicles (HPCMP CREATE<sup>TM</sup>-AV) program and the US Army. The basic CFD meshing approach in Helios is to use a multi-mesh paradigm near-body body-fitted curvilinear or unstructured meshes are used to model rotor components such as blades, hub, fuselage etc., and an off-body Cartesian mesh is used to model the background regions (wakes) away from these components. These meshes form an overset mesh system and a domain connectivity module is used to manage the overset mesh communication among them (Refs. 18, 19).

Helios is capable of using NASA OVERFLOW, NASA FUN3D, and Helios mStrand, a recently developed strand based solver for its near-body mesh (Refs. 8, 20). For its far-field mesh, Helios uses a module called SAMCart, which is capable of adaptive mesh refinement. Specifically, SAMCart implements a 5th order finite-difference spatial discretization and a 2nd-order time-accurate implicit scheme.

Helios is able to interpolate over these flow solvers using its PUNDIT module, which is also responsible for domain

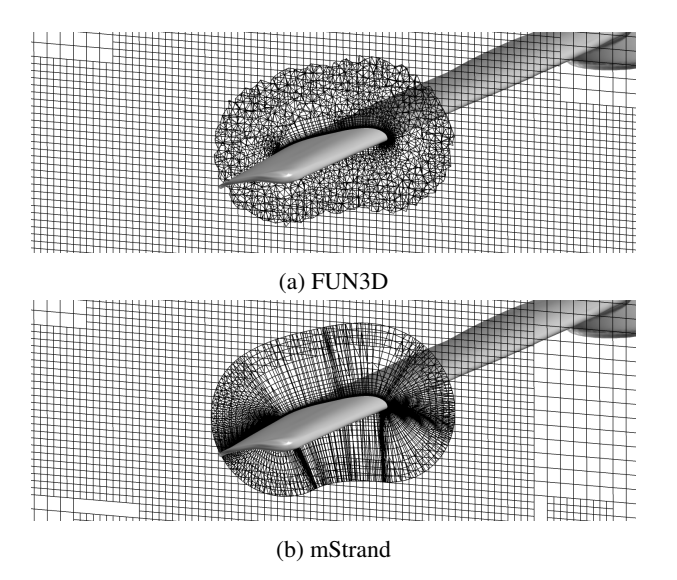


Fig. 4: Overlapping region between the near-body and off-body.

connectivity in parallel computing and implicit hole cutting (Ref. 21). Post processing, including flow field extraction, is performed concurrently with the flow solution computation using CoViz.

#### **Solvers**

In this paper, FUN3D and mStrand are employed for flow solutions in the near-body mesh. FUN3D is NASA's unstructured-grid flow solver that is maintained by researchers at NASA Langley. The overlap between the near-body and off-body meshes is shown in Fig. 4. mStrand is recognized for its ability to automatically generate a near-body volume strand mesh given a watertight surface mesh (Ref. 20). mStrand is maintained by researchers at the Aviation Development Directorate. Both solvers use a 2nd order vertex-centered finite volume discretization.

## Adaptive Mesh Refinement (AMR)

In this study a normalized Q-criterion based on the strain rate tensor, S, and the rotation rate tensor,  $\Gamma$ , is used to determine which regions of the flow domain require additional refinement. The threshold criterion is defined as:

$$f_{threshold} = \frac{1}{2} \left( \frac{||\Gamma^2||}{||S||^2} + 1 \right). \tag{1}$$

Regions of the domain are refined where  $f_{threshold}$  was less than 1. This approach was first proposed by Kamkar et al. (Ref. 22) and has been used across many rotorcraft applications of different scales. In the airfoil and fuselage studies, a steady simulation was run and AMR was turned on from the beginning. In the hover studies, however, AMR is activated in the far field after the first 10 revolutions to allow transient effects to dissipate.

#### **Turbulence models**

In previous quadrotor simulations performed using OVER-FLOW and in most large rotorcraft simulations performed using Helios, regular turbulence models have allowed for prediction of the flow field. It is hypothesized, however, that at the lower Reynolds numbers associated with the small quadrotors, characterization of laminar-turbulence transition is important. Therefore, the performance predictions obtained with transition models that are currently available in Helios v9 are studied. This section provides information about the turbulence models considered in this study.

**Fully Turbulent Models** The two fully turbulent models that are studied in this paper are the Spalart Allmaras (SA) and the  $k-\omega$  shear stress transport ( $k-\omega$ ). The models are coupled with a Detached Eddy Simulation (DES), which is a hybrid model that uses Large Eddy Simulation (LES) to capture regions where the turbulence can be well-resolved by the grid. These models are available in both FUN3D and mStrand.

**Turbulence Transition Models** The four turbulence-transition models available in Helios are briefly described.

The Langtry-Menter model can be utilized with both FUN3D and mStrand (Refs. 23, 24). Previous studies have shown that the model improves computational accuracy for helicopters, but the exploitation of this technique has yet to be accomplished for small quadrotors (Refs. 9, 25). In this study, The Langtry-Menter model is coupled with the k- $\omega$  turbulence model in both FUN3D and mStrand.

Due to the fact that the Langtry-Menter transition model was traditionally coupled to the computationally intensive 2-equation k- $\omega$  model, Medida et al. developed an adaptation of this model that would work with the 1-equation SA model. More details can be found in Medida et al's paper (Ref. 26) in which they revise some of the original correlation coefficients to better fit the new implementation. In this study, the Medida-Baeder transition model is referred to as MB, and is currently only available in mStrand.

Menter et al. published an updated version of the Langtry-Menter transition model in which some of the deficiencies of the older model have been addressed (Ref. 27). In this model, Menter et al. was also able to simplify some of the transition correlations in order to reduce the total number of transition equations from two to one, thereby making the model less computationally expensive. In this study, the Menter 2015 model is coupled with the k- $\omega$  turbulence model in mStrand, and referred to as M15.

The Coder amplification factor transport transition model, referred to as AFT, is a two equation, phenomenological model that is based on boundary layer growth. Coder et al. describes the original implementation as well as enhancements to the methodology, which are used in this work, in their papers (Refs. 28,29). In this study, the Coder amplification factor transport model is coupled with the SA turbulence model in mStrand.

#### AIRFOIL STUDIES

In order to alleviate the need for an in-depth mesh dependence study for the entire quadrotor for each simulation method, first a grid study for just an airfoil, representative of the DJI Phantom 3, is performed. Then, a rectangular wing with this same airfoil cross section is considered.

The airfoil is taken from the three-quarters rotor span for this study. The airfoil chord length is 0.0166 m and the angle of attack in hover is about  $8^{\circ}$ . The freestream flow at the three-quarters blade span for 5000 RPM is 47 m/s. The Reynolds number is thus around 53000.

All available turbulence models were implemented to ensure that the grid convergence was model-independent as well.

#### 2D Airfoil

In the 2D cases, the trailing edge and leading edge spacing was kept at a constant 0.0001c and 0.0002c, respectively, but the number of points around the airfoil was varied. The simulations were conducted in mStrand with the off-body region turned off. The surface mesh was generated during run time from the given airfoil coordinates. The volume was extruded to approximately 50 times the chord length, and the wall spacing was generated such that  $y^+ < 1$ . The simulations were run as steady cases and run for  $10^5$  steps, with the converged result calculated as the average of the last 1000 steps. The convergence results of these simulations are plotted in Fig. 5. The grid convergence for the airfoil is almost identical across all turbulence models suggesting transition effects are not important for the 2D simulations.

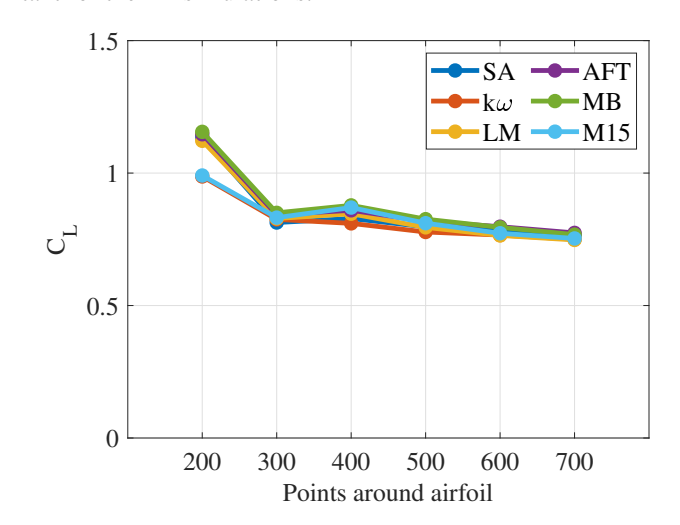


Fig. 5: 2D airfoil lift coefficient results.

#### 3D Wing

In the 3D cases, the trailing edge and leading edge spacing were kept the same as the 2D cases. A 12 cm span wing was created to match the rotor blade radius giving an aspect ratio of approximately 7. The surface gridding methodology is different from the 2D cases because of the unstructured nature of

the solvers. The surface mesh was generated using Pointwise and ranged from  $3.0*10^4$  to  $2.3*10^5$  points, corresponding to surface spacings between 0.075c to 0.02c. However, although the surface meshes used in both solvers are identical, the FUN3D volume mesh must be provided to the solver beforehand. The mStrand mesh, on the other hand, was generated at run time by specifying desired spacing properties. In both solvers, the near body volume mesh had a wall spacing that satisfied  $y^+ < 1$  and extended to 0.8 times the chord length. Both FUN3D and mStrand were used and coupled to the off-body solver SAMCART. The off-body volume mesh was extruded to approximately 50 times the chord length.

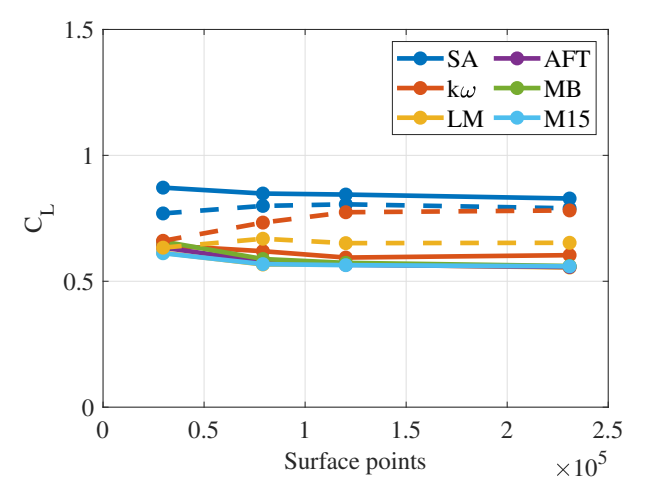


Fig. 6: 3D airfoil lift coefficient results (solid lines correspond to mStrand, dashed lines correspond to FUN3D).

The simulations were run as steady cases for 10<sup>5</sup> steps, with the converged result calculated as the integrated lift from the wing over the last 10<sup>3</sup> steps. In Fig. 6, the results of the 3D wing study are plotted for all transition models tested. Based on these studies alone, the fully turbulent models seem to predict higher coefficient of lift than the transition models, which will affect how thrust is produced during the isolated rotor cases. In addition, there is a noticeable difference in the convergence results from the 2D cases. In the 3D cases, although each model alone demonstrates good grid convergence, the models do not converge to the same value.

The pressure on the surfaces of the wings from the FUN3D simulations was plotted in Fig. 7. The upper parts of the pictures correspond to the leading edge. The pressures on the wing reveal that the lift distribution is smooth for the fully turbulent cases, but erratic for the transition case. In addition, the flow on the leading edge remains attached for the turbulent cases, but not for the transition cases, which explains the loss of lift. The asymmetry in the spanwise direction seems unphysical although it is known that turbulence is a three-dimensional phenomenon. Similar results can be seen in the mStrand solver, with the exception of the k- $\omega$  case, which behaves similar to the transition models in these studies. It is clear that more work needs to be done to determine the accuracy of the transition models for a simple configuration like the rectangular wing. This will be the focus of future studies.

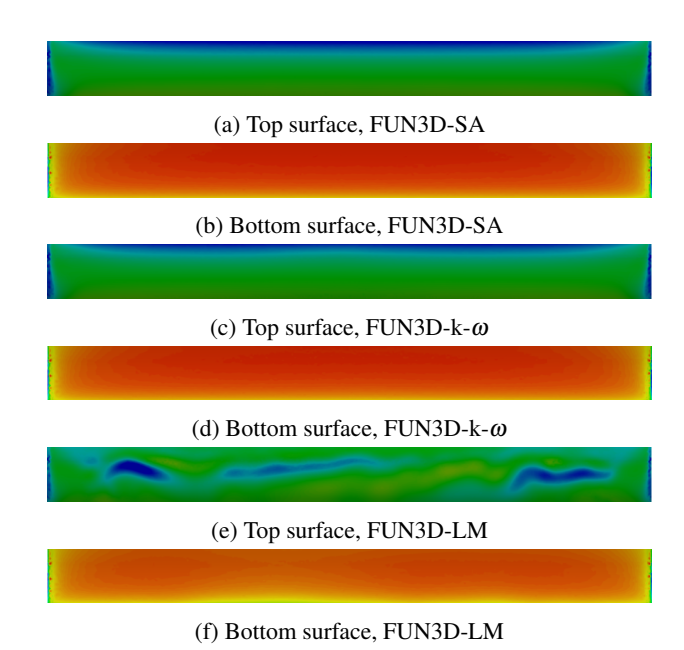


Fig. 7: Instantaneous pressure on the 3D wing at the final step. Red indicates high pressure and blue indicates low pressure.

Based on the results of the convergence study, the mesh generated for the wing with a  $1.2*10^5$  surface points, equivalent to a surface spacing of 0.03c, was deemed sufficient for capturing the flow effects. Therefore, the same grid properties were used for the isolated rotor cases. A picture of the mesh at the tip of the rotor can be found in Fig. 8, and the properties in Table 2.

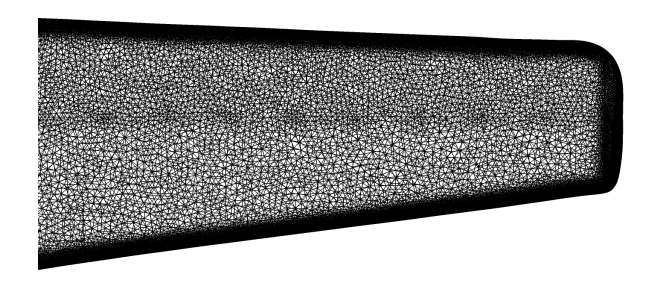


Fig. 8: Rotor tip mesh.

Table 2: DJI Phantom 3 rotor mesh properties.

Dimension
0.12 m.
0.03c
0.0002c
0.0001c
0.03c
1.1
0.4c

#### ISOLATED ROTOR STUDIES

Isolated rotor unsteady simulations were conducted at 3000, 5000, and 7000 RPM for the various turbulence models in both mStrand and FUN3D. The mStrand mesh was set up to extrude 31 cells normal to the surface at run time. The nearbody mesh in mStrand had approximately 0.5 million surface points and 16 million volume points. The near-body mesh in FUN3D used the same surface mesh as mStrand, but a coarser volume mesh that contained 9 million points. The first near body wall spacing in both solvers was set to 0.0001c, which was derived from the 3D wing studies and satisfies  $y^+ < 1$ . In general the off-body adaptive Cartesian mesh had around 48 million points. The first 10 rotor revolutions are run with a 2.5 azimuth time step, corresponding to 1440 total time steps. The final 3 rotor revolutions are run with a 0.25 azimuth time step, equivalent to 4320 time steps. Therefore, the isolated rotor studies are conducted with a total of 5760 time steps.

## Convergence

In order to extract a reliable prediction from the simulation, the solution must approach a steady state value. A plot of the convergence of thrust over the entire simulation for the 7000 RPM cases can be found in Fig. 9. There is an initial adjustment to transient effects during the first 10 rotor revolutions but, when the time stepping methodology is adjusted, the oscillations become less noisy and more steady. This graph is representative of the temporal convergence for the other RPMs, which are not plotted. The converged thrust and moment values are calculated as the average over the last rotor revolution.

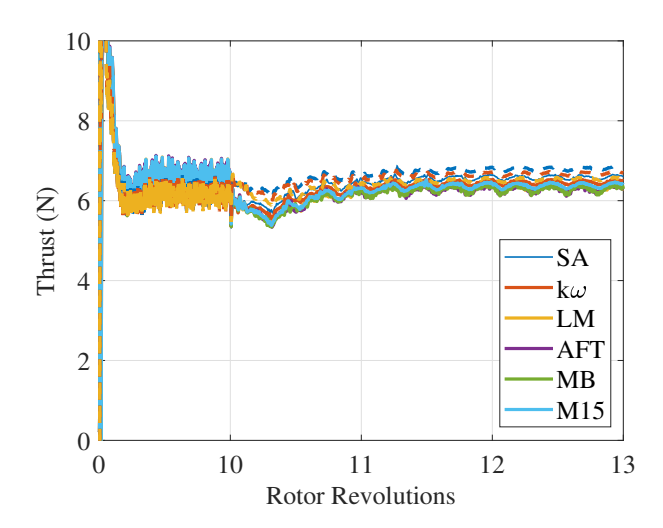


Fig. 9: Thrust convergence at 7000 RPM (solid lines correspond to mStrand, dashed lines correspond to FUN3D).

#### Results

The isolated rotor thrust results from mStrand are plotted in Figs. 10a, 10c, and 10e, while the isolated rotor thrust results from FUN3D are plotted in Figs. 10b,10d, and 10f. The black

lines represent the experimental thrust values measured by Russell et al. and include the reported uncertainty (Ref. 17). Russell et al. reported an 0.596 N uncertainty in the thrust and a 0.0217 N-m uncertainty in the moment about the rotor axis (Ref. 17).

The trends of the 3D wing studies, which represented the induced velocity at 5000 RPM, generally hold true in the isolated rotor studies. The thrust produced by the SA model is greater than that of the k- $\omega$  model. The transition models all perform similarly and give lower thrust values than the SA and k- $\omega$  models, with the exception of the FUN3D-LM model at 7000 RPM. Based on these mStrand results, the M15 model provides demonstrably different results than the LM model at higher RPMs. The FUN3D fully turbulent models gives higher than expected thrust at 7000 RPM just as with mStrand.

All of the models give the expected thrust value within the experimental uncertainty. Therefore, based on the thrust predictions, none of these models has preference over others. The iso-surfaces of Q-criterion for the 7000 RPM cases are shown, colored by vorticity magnitude, for the various solvers and models in Fig. 11. The inclusion of turbulence transition generally shows finer vortical braids in the wake, both in the FUN3D and mStrand flow solutions. This is likely due to increased AMR activity, but the root cause is still under investigation.

Another performance metric for rotorcraft is the figure of merit, a measure of the ratio of the actual power output to the ideal power output from a rotor. The figure of merit is calculated as:

$$\eta = \frac{C_T^{3/2}}{\sqrt{2}C_O}. (2)$$

In . 2, the thrust coefficient  $C_T$  is defined as:

$$C_T = \frac{T}{\rho A \Omega^2 R^2}. (3)$$

The torque coefficient  $C_Q$  is defined as:

$$C_{Q} = \frac{M}{\rho A \Omega^{2} R^{2}}.$$
 (4)

The isolated rotor figure of merit is plotted in Fig. 12. The simulations do not predict the figure of merit well, but it is clear from the studies that the fully turbulent SA model is closest among both solvers. Interestingly, although the k-\omega model is also fully turbulent, it does not agree with the other fully turbulent models. These findings could be related to the results of the 3D wing studies in which mStrand-k-\omega predicted a lower lift coefficient than the other fully turbulent models, indicating possible deficiencies in this specific configuration. It should again be noted that, although the accuracy of the results are compared using the reported experimental value, all of the results agree within the error range.

## Computational time

Another important consideration in CFD is the amount of available computational resources. The calculations were all

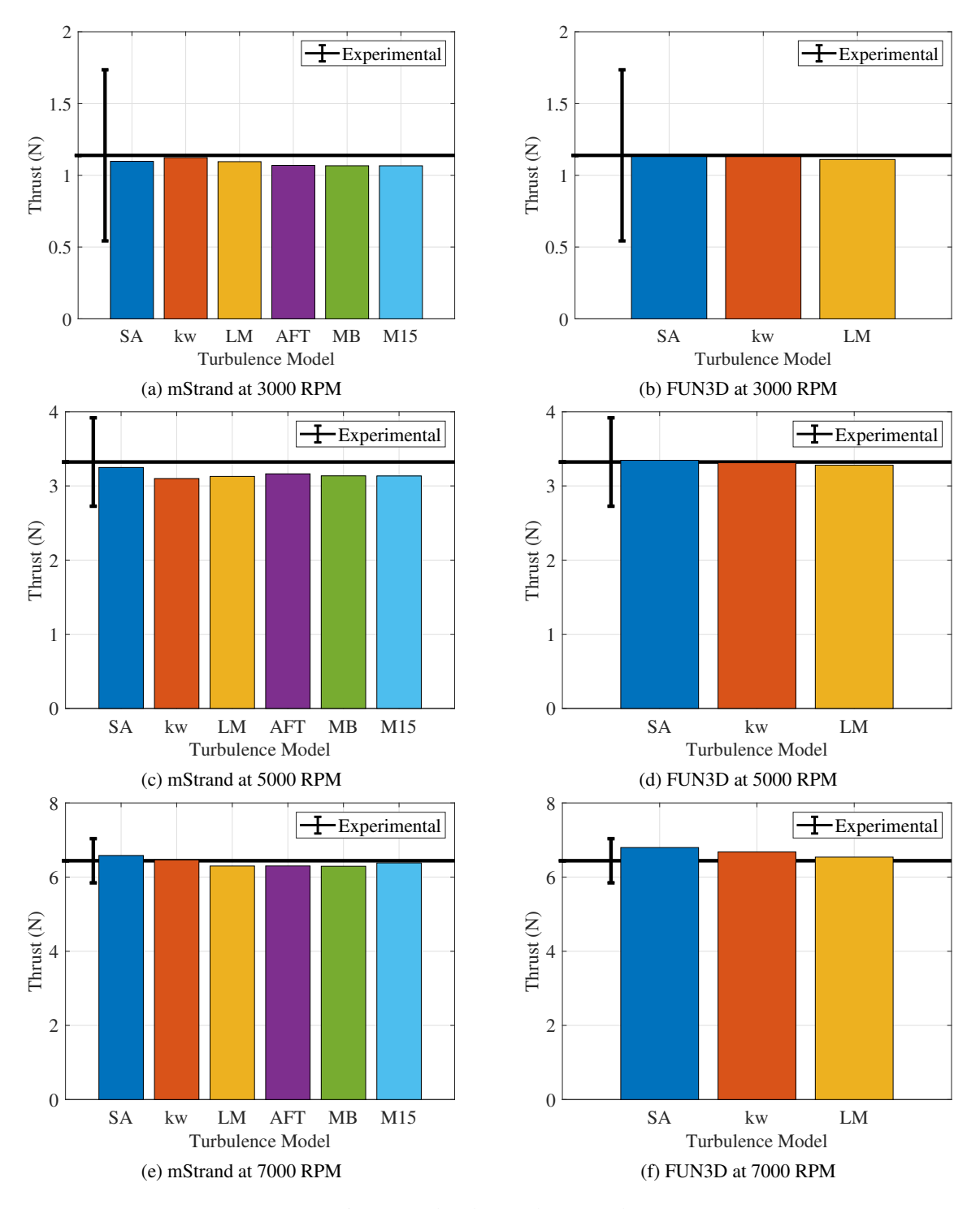


Fig. 10: Isolated rotor thrust results.

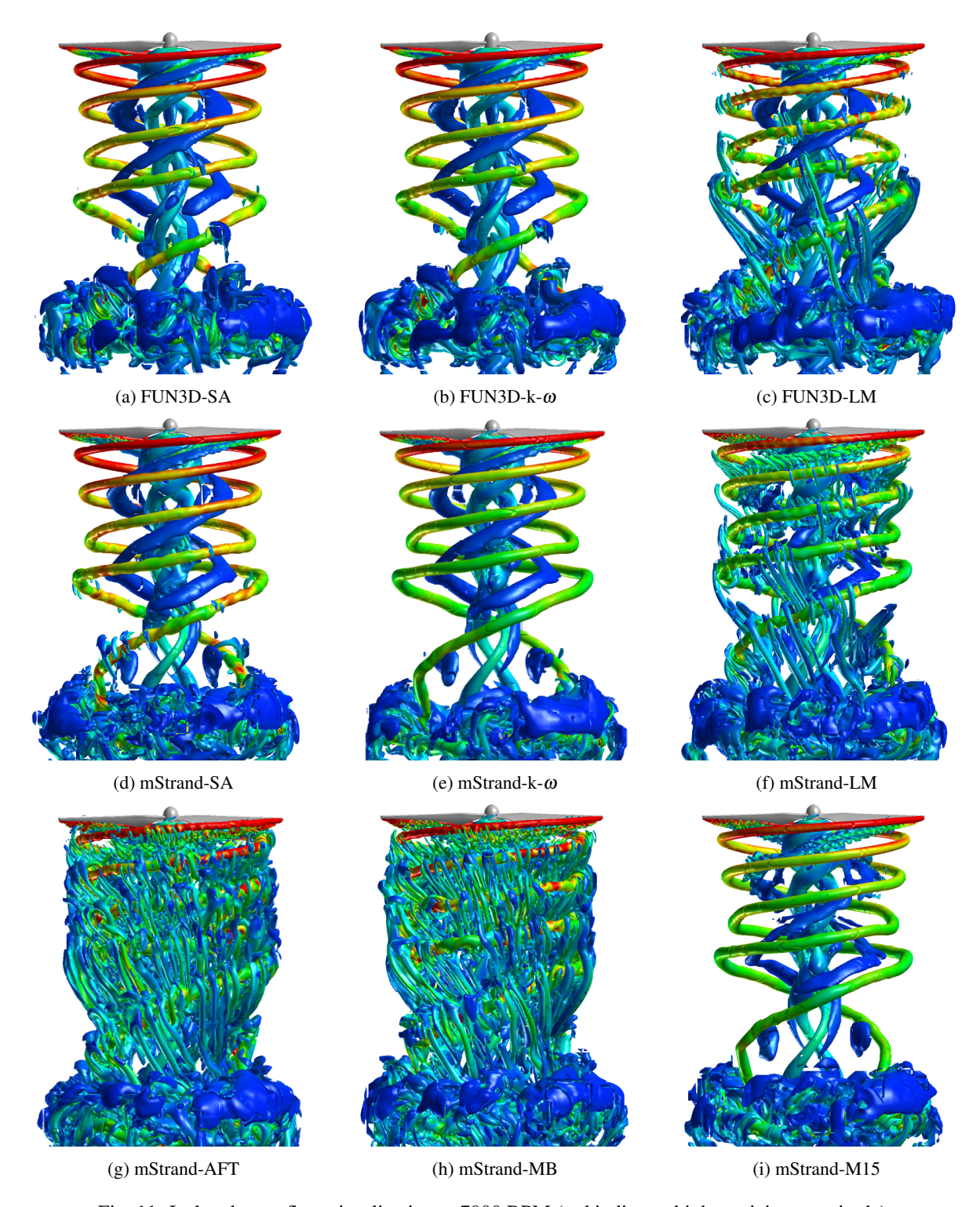


Fig. 11: Isolated rotor flow visualization at 7000 RPM (red indicates high vorticity magnitude).

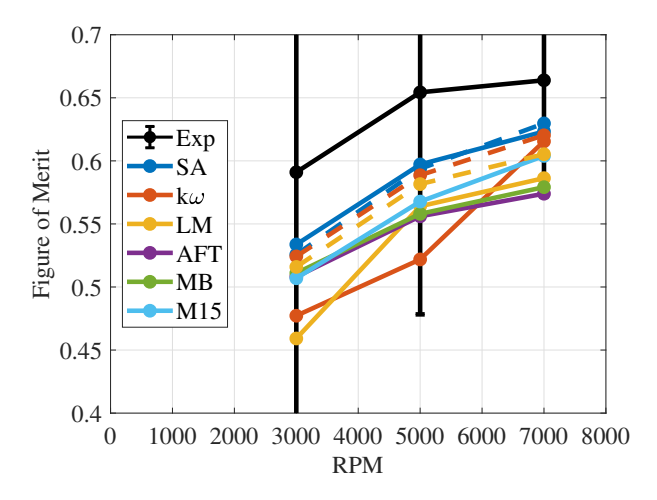


Fig. 12: Isolated rotor figure of merit results.

performed on the Department of Defense High Performance Computing (DoDHPC) cluster Conrad. A total of 800 processors were used for the isolated rotor cases.

A plot of the computation time per time step for the isolated rotor studies can be seen in Fig. 13. The FUN3D cases typically ran faster than the mStrand, and the FUN3D-SA combination is the fastest overall. The main difference in the timing comes from the AMR part of the simulation. The average number of points in the off-body mesh is greatest at 5000 RPM, which correlates with the increased computational time at this rotor speed.

The isolated rotor simulations show that all of the turbulence models provide reasonable thrust predictions; the figure of merit predictions show that all of the methods are lacking but that the SA model is best; the computational efficiency criteria shows that SA is the best. Therefore, the quadrotor simulations were carried out using the SA model.

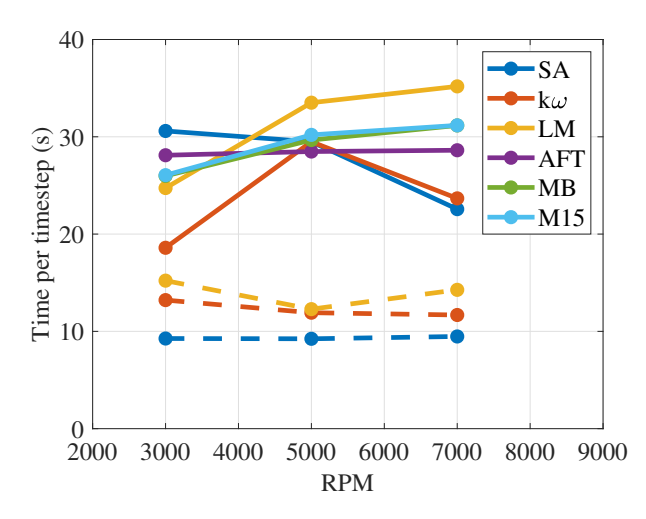


Fig. 13: Computation time per time step for the isolated rotor studies (solid lines correspond to mStrand, dashed lines correspond to FUN3D).

Table 3: DJI Phantom 3 fuselage mesh properties.

Property	Dimension	
Length (along arm)	0.39 m.	
Surface spacing	0.05c	
Volume spacing	0.05c	
Normal growth rate	1.3	
Trim distance	0.4c	

## **FUSELAGE STUDIES**

While the NASA Ames study (Refs. 16, 17) did obtain lift and drag values on the fuselage, their report did not simulate freestream flow on the top of the fuselage, which is typical of the rotor wake in hover and represents download. Therefore, a grid study that focuses on convergence for the steady flow values of download on the fuselage was completed.

The flow freestream was setup to simulate rotor downwash on the fuselage at 15 m/s. The mesh independence plot with download as the convergence variable can be seen in Fig 15. After the first mesh refinement, the download is relatively unchanged. The FUN3D and mStrand results seem to agree well throughout the entire study. Due to the lack of mesh dependence, a coarser mesh, containing approximately  $1.5*10^5$  surface points, was determined to be appropriate for the quadrotor studies. More details on the fuselage mesh can be found in Table 3. A picture of the final mesh used can be seen in Fig. 14.



Fig. 14: Fuselage mesh.

# **QUADROTOR STUDIES**

The grids that were used in the isolated rotor and fuselage studies were combined to create the grids for the full quadrotor simulations. Quadrotors typically have adjacent counterrotating rotors and opposing co-rotating rotors to provide an inherent torque balance. The rotor grids used in the study are identical when mirrored. In general the off-body mesh contained 180 million points total.

The SA model with FUN3D was chosen for the full quadrotor simulation. To compare with the isolated rotor studies, the same RPM sweep was run at 3000, 5000, and 7000 RPM. However, to compare with experimental values, an additional case was run at 3500 RPM. The same time stepping methodology of the isolated rotor cases, in which 10 revolutions are run at 2.5 azimuth and 3 revolutions are run at 0.25 azimuth, is followed.

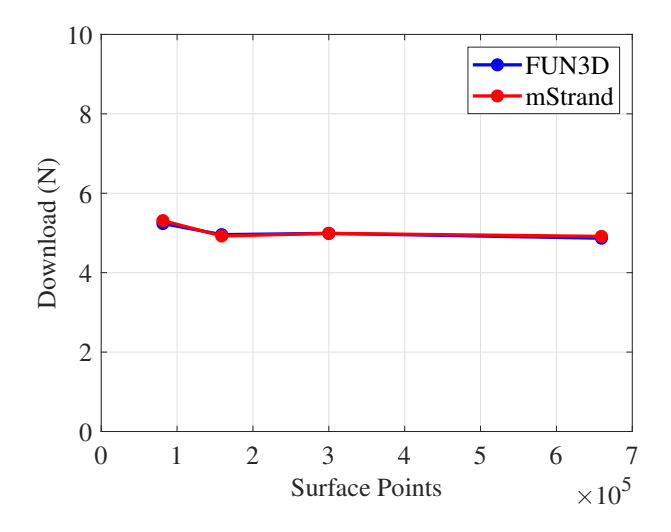


Fig. 15: Grid convergence for the fuselage.

#### Convergence

The convergence of thrust for the quadrotor cases can be seen in Fig. 16. As expected, due to the higher turbulence levels from the increase in the Reynolds numbers, there are larger oscillations in thrust values for the higher RPM cases. However, by the final rotor revolution, the unsteadiness becomes periodic and is assumed to have escaped transient effects. Similar to the isolated rotor studies, the converged thrust is determined as the average of the final rotor revolution.

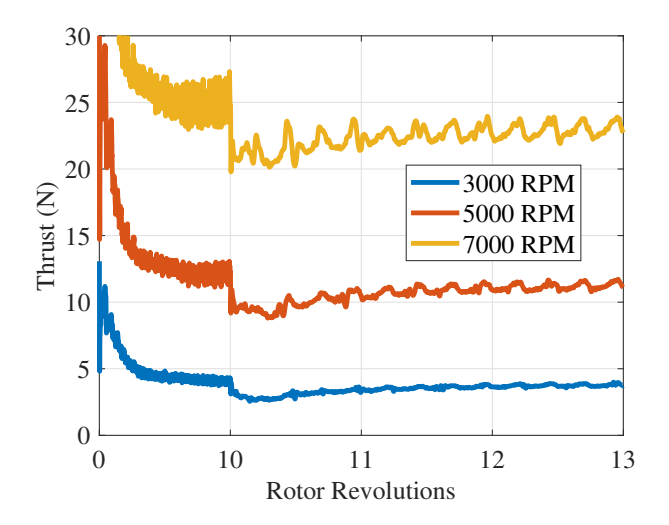


Fig. 16: Quadrotor thrust convergence.

#### Results

The quadrotor thrust results are plotted against experimental data in Fig. 17. The results seem to agree well overall. However, the trend for the quadrotor is slightly different than that seen for the isolated rotor with the thrust falling off a bit from the expected value at the higher RPMs. Aerodynamic interactions between the rotor and the fuselage not being resolved well may be responsible for this outcome.

To characterize the various aerodynamic effects, the quadrotor thrust results at each RPM were normalized by the pre-

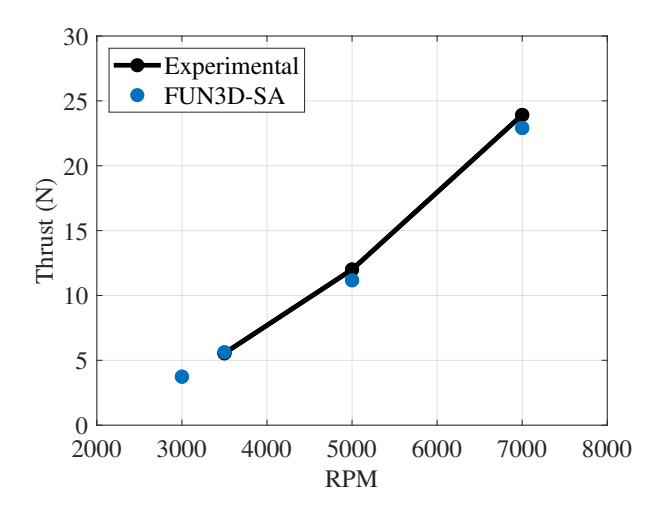


Fig. 17: Quadrotor thrust results.

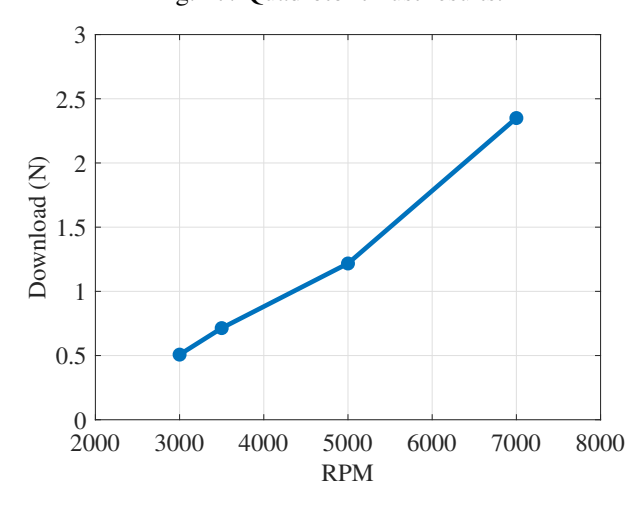


Fig. 18: Quadrotor download results.

dicted thrust from the isolated rotor, and plotted in Fig. 19. The thrust produced by the rotor blades is separated from the total thrust, so the data includes values that either include or exclude the download on the fuselage. As expected, the thrust from the four rotors is less than four times the single rotor thrust. When fuselage download is included, the overall thrust reduces even further. In addition, although there is no experimental data for comparison, the quadrotor download is plotted in Fig. 18.

To serve as another benchmark for performance comparisons, the figure of merit of the quadrotor was also computed. The figure of merit comparison between the quadrotor and isolated rotor configurations is plotted in Fig. 20. The figure of merit for the quadrotor was calculated using the total blade area from all four blades and the sum of the absolute values of the rotor moments. The figure of merit of the quadrotor is less than that of the isolated rotor across all RPMs, suggesting that the total thrust of the vehicle is limited by the download. However, the figure of merits for both configurations are closest at 3000 RPM, suggesting that the interactions are not as significant at lower Reynolds numbers.

To visualize the flow field, the iso-surfaces of Q-criterion for the 3000, 5000, and 7000 RPM cases were plotted, colored by

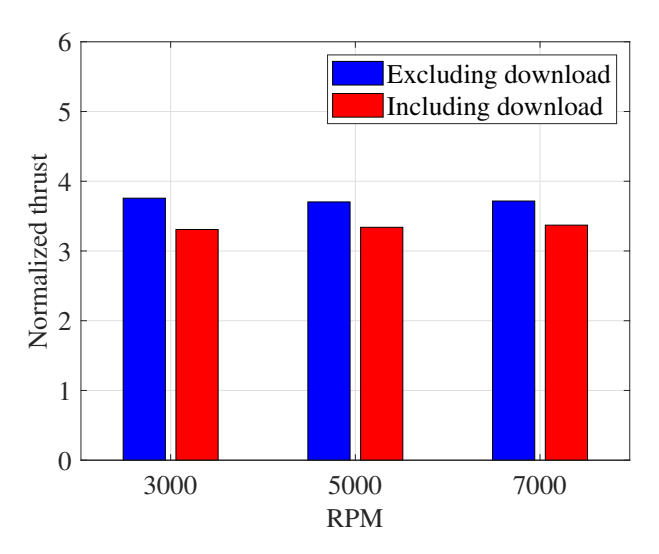


Fig. 19: Quadrotor thrust results normalized by isolated rotor results.

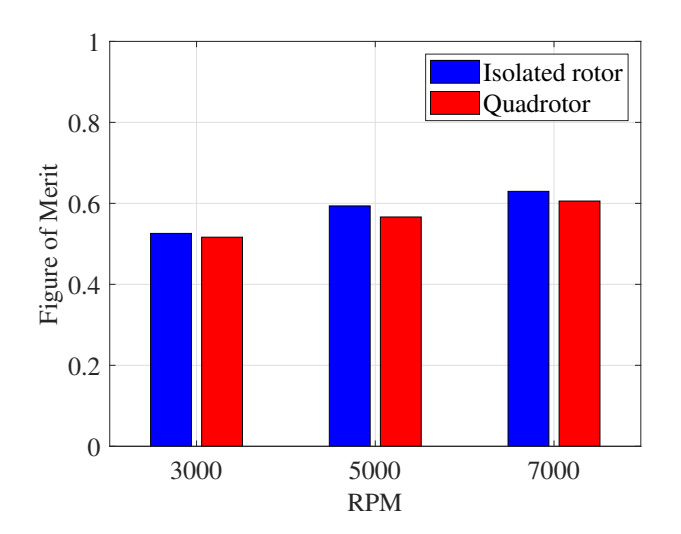


Fig. 20: Isolated rotor vs quadrotor figure of merit.

vorticity magnitude, in Figs. 21-22. There are no noticeable differences in the vortical structures of the rotor wake, but the overall vorticity increases with RPM, as expected due to higher Reynolds numbers.

#### Computational time

The full quadrotor calculations were also performed on the DoDHPC cluster Onyx. A total of 880 processors were used. A bar graph of the time spent per time step by each module throughout the quadrotor simulations can be seen in 23. Generally, the time required increased with the RPM. This may be due to the fact that, as the Reynolds number increases, the amount of vorticity increases. Therefore, the adaptation process flagged more regions of the flow domain, causing the off body mesh to increase in size and consume more time. The overset mesh operations, in which iBlanks and fringe cells are discovered, consumed most of the simulation time.

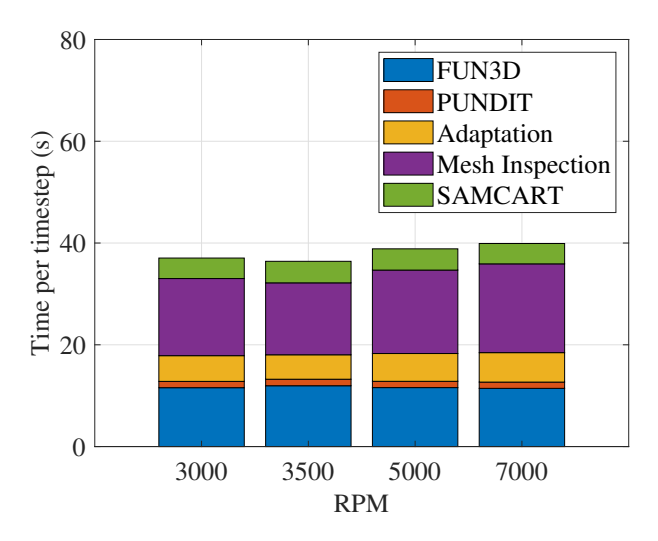


Fig. 23: Time spent during FUN3D quadrotor simulations.

## **CONCLUSION**

Computational Fluid Dynamics simulations of the DJI Phantom 3 were conducted on the DoDHPC clusters to benchmark the use of the rotorcraft code CREATE<sup>TM</sup>-AV Helios for small quadrotor simulations. To broaden the scope of the research, two different unstructured near-body solvers were used: NASA FUN3D and Helios mStrand. The newly available transition modeling capabilities of Helios were also tested in this study.

At the start of the study, the three-quarters span of the rotor blade was extracted to generate a 2D airfoil and related 3D rectangular wing for use in grid convergence studies. Freestream flow was simulated based on the expected velocity at 5000 RPM. The lift coefficient was studied as it directly relates to thrust. The 2D cases were run in mStrand with all available turbulence models. In this study, the models all converged to the same value as the grid count increased, and demonstrated low mesh dependence. The 3D cases were run with both FUN3D and mStrand, and, although the mesh independence was also observed in the 3D case, the converged lift coefficient did not agree across the models. In general, the fully turbulent models predicted higher lift values than the transition models.

Next, the appropriate grid spacing derived from the wing study was used to generate isolated rotor meshes. Hover simulations of the isolated rotor were conducted for all available models in both solvers. The models all performed well in accurately predicting thrust, but the high computational efficiency of the fully turbulent 1-equation Spalart Allmaras model made it the clear choice for the full quadrotor simulations.

A grid sensitivity study of download on an isolated fuselage simulations was conducted to determine the appropriate mesh sizing for resolving the downwash on the fuselage.

Finally, full quadrotor simulations, consisting of all four rotors and the fuselage, were conducted using NASA FUN3D

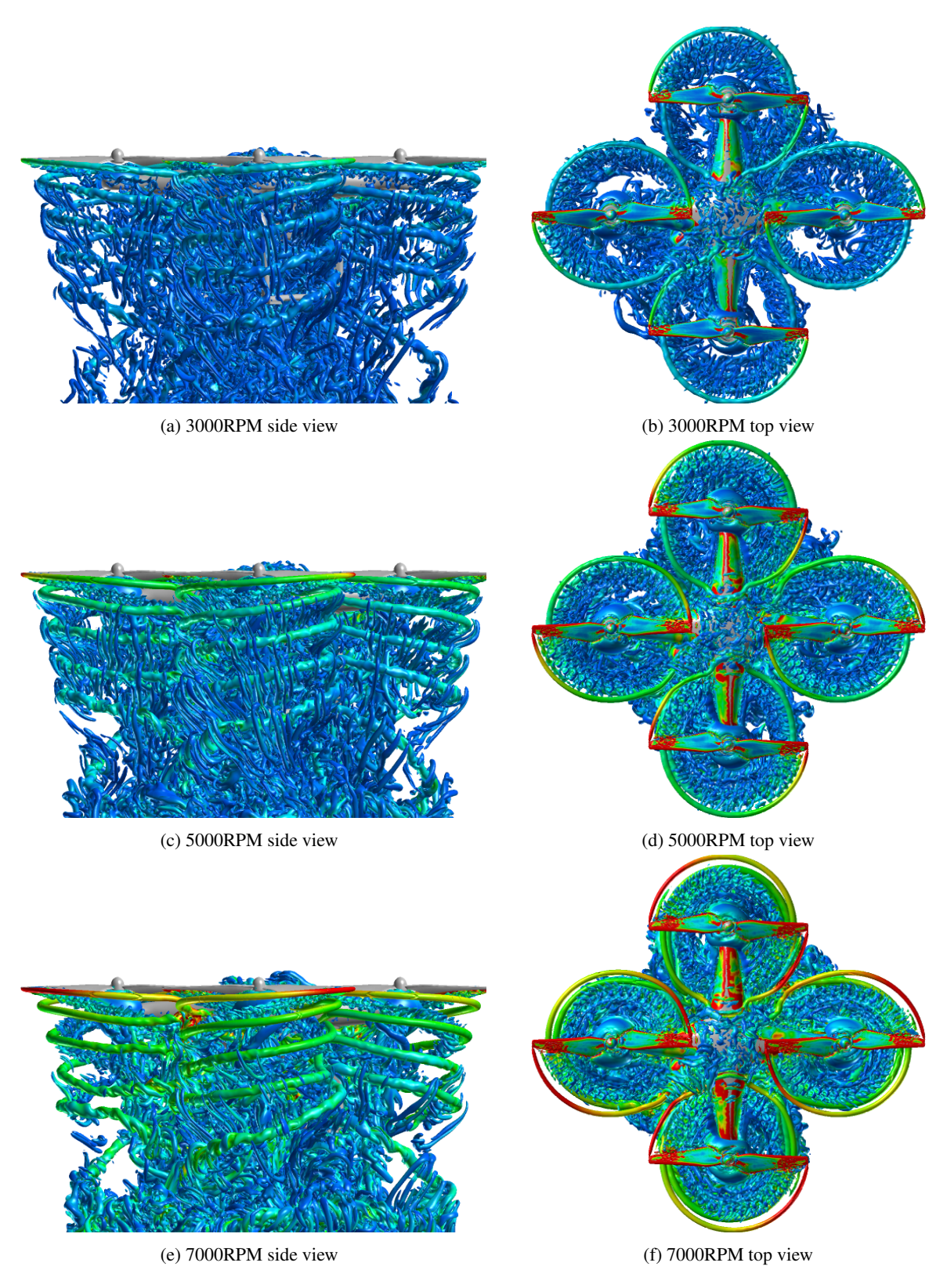


Fig. 21: Full quadrotor flow visualization (red indicates high vorticity magnitude).

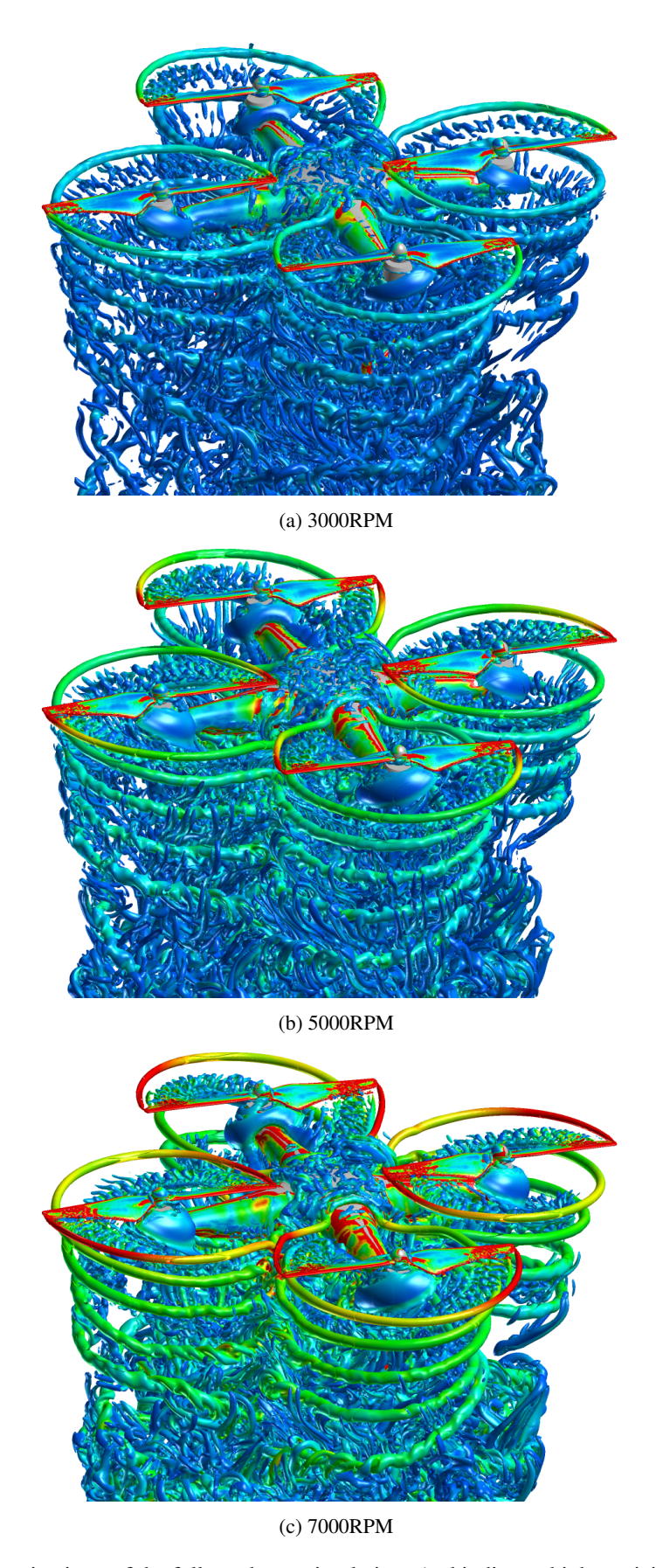


Fig. 22: Isometric views of the full quadrotor simulations (red indicates high vorticity magnitude).

and the Spalart Allmaras model. Good agreement with experimental thrust values was found over the entire RPM range. The flow visualization of the various cases yielded insight into the increasing vorticity magnitude with RPM. The computed figure of merit for both the isolated rotor and full quadrotor simulations did not agree well with experimental results, indicating a need for a better grid dependence study or improvements in turbulence modeling.

This study demonstrates the capability of the CREATE<sup>TM</sup>-AV Helios computational methodology for small rotorcraft, and serves as validation of the suite of codes to enable further computational investigation for small multirotor systems.

#### **FUTURE WORK**

Due to the uncertainty of the experimental data, the thrust prediction alone was not a good metric for the accuracy of the turbulence models. However, the underprediction of the figure of merit indicates a need for modeling improvements for measuring torque. In addition, an in-depth study of the DJI Phantom 3, in which the turbulence transition location is measured, must be conducted to better grasp the validity of the models. The potential computational work extends beyond aerodynamic calculations. As these vehicles are integrated into society, the aeroacoustics of these quadrotors must also be characterized. In the past, CFD has been coupled to aeroacoustics codes to predict sound. The turbulence models have been shown in this study to affect the wake generation, which will, in turn, affect sources of noise such as blade vortex interaction.

Finally, although it is important to characterize quadrotor performance in hover, the flow effects change drastically in forward flight. The Reynolds numbers on the rotor blades will increase, and the unsteadiness can yield transitional effects. However, there is currently a lack of knowledge in the literature on the quadrotor trimmed flight. Although coupled helicopter CFD predictions have been successful in the past, quadrotors typically fly by changing the RPM of the rotor blades. To the knowledge of the authors, there have been no CFD studies of a quadrotor in RPM-based trimmed flight. RPM-based trim is a newly added capability in Helios and is discussed in detail by Roget et al (Ref. 30). Mr. Thai will be continuing the Helios quadrotor validation work this summer by studying RPM-based trim for quadrotors with the Aviation Development Directorate at NASA Ames Research Center.

Author contacts: Austin Thai adthai@bu.edu Sheryl Grace sgrace@bu.edu

#### ACKNOWLEDGMENTS

Dr. Roger Strawn of the U.S. Army Aviation Development Directorate granted allocation on the Department of Defense High Performance Computing systems. Carl Russell of NASA Ames Research Center provided CAD geometry of the rotor and fuselage as well as experimental data from his technical report. Vinod Lakshminarayan, the developer

of mStrand, provided a lot of feedback with regards to running mStrand simulations. Mr. Thai receives funding from NSF Award 1728277: Control of Micro Aerial Vehicles under Aerodynamic and Physical Contact Interactions and from the Boston University Mechanical Engineering department.

#### REFERENCES

<sup>1</sup>Walmart, "DJI Phantom 3 Standard Drone". https://www.walmart.com/ip/DJI-Phantom-3-Standard-Drone/48748668, accessed April 2019.

<sup>2</sup>Hwang, J. Y., Jung, M. K., and Kwon, O. J., "Numerical Study of Aerodynamic Performance of a Multirotor Unmanned-Aerial-Vehicle Configuration," *Journal of Aircraft*, Vol. 52, (3), May. 2015, pp. 839–846.

<sup>3</sup>Misiorowski, M., Gandhi, F., and Oberai A. A., "A Computational Study on Rotor Interactional Effects for a Quadcopter in Edgewise Flight," American Helicopter Society 74th Annual Forum, Phoenix, AZ, May 2018.

<sup>4</sup>Yoon, S., Diaz, P., Boyd, D. D. Jr., Chan, W. M., and Theodore C. R. "Computational Aerodynamic Modeling of Small Quadcopter Vehicles," American Helicopter Society 73rd Annual Forum, Fort Worth, TX, May 2017.

<sup>5</sup>Diaz, P. V., and Yoon, S., "High-Fidelity Computational Aerodynamics of Multi-Rotor Unmanned Aerial Vehicles," 2018 AIAA Aerospace Sciences Meeting, Kissimmee, FL, January 2018.

<sup>6</sup>Christian, A., Boyd, D. D. Jr., Zawodny, N. S., and Rizzi, S. A., "Auralization of tonal rotor noise components of a quadcopter flyover," Inter-Noise 2015, San Francisco CA, August, 2015.

<sup>7</sup>Zawodny, N. S. and Boyd, D. D. Jr., and Burley, C.L., "Acoustic Characterization and Prediction of Representative, Small-Scale Rotary-Wing Unmanned Aircraft System Components," American Helicopter Society 72nd Annual Forum, West Palm Beach, FL, May, 2016.

<sup>8</sup>Jain, R., Biedron, R. T., Jones, W. T., and Lee-Rausch, E. M., "Modularization and Validation of FUN3D as a CREATE-AV Helios Near-body Solver," 54th AIAA Aerospace Sciences Meeting, San Diego, CA, January 2016.

<sup>9</sup>Jain, R., "Hover Predictions on the S-76 Rotor with Tip Shape Variation Using Helios," *Journal of Aircraft*, Vol. 55 (1), 2018, pp. 66–77.

<sup>10</sup>Sheng, C., Wang, J., and Zhao, Q., "Improved Rotor Hover Predictions Using Advanced Turbulence Modeling," *Journal of Aircraft*, Vol. 53 (5), 2016, pp. 1549–1560.

<sup>11</sup>Tran, S., Lakshminarayan, V., Sitaraman, J., and Wissink, A., "Transition Modeling in HPCMP CREATETM-AV Helios v9," AIAA Scitech 2019 Forum, San Diego, CA, 2019.

- <sup>12</sup>Sheng, C., "Role of Transition Modeling in Rotor Hover Predictions," *Journal of Aircraft*, Vol. 55 (1), 2018, pp. 23–37.
- <sup>13</sup>Katz, A., Wissink, A. M., Sankaran, V., Meakin, R. L., and Chan, W. M. "Application of Strand Meshes to Complex Aerodynamic Flow Fields" *Journal of Computational Physics*, Vol. 230 (17), 2011, pp. 6512–6530.
- <sup>14</sup>Meakin, R. L., Wissink, A. M., Chan, W. M., Pandya, S. A., Sitaraman, J., "On Strand Grids for Complex Flows," 18th AIAA Computational Fluid Dynamics Conference, Miami, FL, 2007.
- <sup>15</sup>Wissink, A. M., Katz, A. J., Chan, W. M., and Meakin, R. L., "Validation of the Strand Grid Approach," 19th AIAA Computational Fluid Dynamics Conference, San Antonio, TX, 2009.
- <sup>16</sup>Russell, C., Willink, G., Theodore, C., Jung, J.and Glasner, B., "Wind Tunnel and Hover Performance Test Results for Multicopter UAS Vehicles," American Helicopter Society 72nd Annual Forum, West Palm Beach, FL, May 2016.
- <sup>17</sup>Russell, C., Jung, J., Willink, G., and Glasner, B., "Wind Tunnel and Hover Performance Test Results for Multicopter UAS Vehicles," NASA TM 219758, 2018.
- <sup>18</sup>Sankaran, V., Wissink, A., Datta, A., Sitaraman, J., Jayaraman, B., Potsdam, M., Katz, A.,Kamkar, S., Roget, B., Mavriplis, D., Saberi, H., Chen, W., Johnson, W., and Strawn, R., "Overview of the Helios Version 2.0 Computational Platform for Rotorcraft Simulations," 49th AIAA Aerospace Sciences Meeting, Orlando, FL, January 2011.
- <sup>19</sup>Wissink, A., Jayaraman, B., Datta, A., Sitaraman, J., Potsdam, M., Kamkar, S., Mavriplis, D., Yang, Z., Jain, R., Lim, J., and Strawn, R., "Capability Enhancements in Version 3 of the Helios High-Fidelity Rotorcraft Simulation Code," 50th AIAA Aerospace Sciences Meeting, Nashville, TN, January 2012.
- <sup>20</sup>Roget, B., Sitaraman, J., Lakshminarayan, V., and Wissink, A., "Prismatic Mesh Generation Using Minimum Distance Fields," Tenth International Conference on Computational Fluid Dynamics, Barcelona, Spain, 2018.
- <sup>21</sup>Sitaraman, J., Floros, M. W., Wissink, A. M., and Potsdam, M., "Parallel Domain Connectivity Algorithm for Unsteady Flow Computations Using Overlapping and Adaptive Grids," *Journal of Computational Physics*, Vol. 229 (12), 2010, pp. 4703–4723.
- <sup>22</sup>Kamkar, S., Wissink, A., Sankaran, V., and Jameson, A., "Feature-driven Cartesian adaptive mesh refinement for vortex-dominated flows," *Journal of Computational Physics*, vol. 230, 2011, pp. 6271–6298.
- <sup>23</sup>Langtry, R. B. and Menter, F. R., "Correlation-Based Transition Modeling for Unstructured Parallelized Computational Fluid Dynamics Codes," *AIAA Journal*, Vol. 47, (12), 2009, pp. 2894–2906.

- <sup>24</sup>Menter, F. R., Langtry, R. B., and Volker, S., "Transition Modelling for General Purpose CFD Codes," *Flow, Turbulence and Combustion*, Vol. 77, (1), 2006, pp. 277–303.
- <sup>25</sup>Richez, F., Nazarians, A., and Lienard, C., "Assessment of Laminar-Turbulent Transition Modeling Methods for the Prediction of Helicopter Rotor Performance," 43rd European Rotorcraft Forum, Milano, Italy, 2017.
- <sup>26</sup>Medida, S., and Baeder, J., "Application of the Correlation-based Gamma-Re Theta t Transition Model to the Spalart-Allmaras Turbulence Model," 20th AIAA Computational Fluid Dynamics Conference, Honolulu, HI, 2007.
- <sup>27</sup>Menter, F. R., Smirnov, P. E., Liu, T., and Avancha, R., "A One-Equation Local Correlation-Based Transition Model," *Flow, Turbulence and Combustion*, vol. 95, (4), 2015, pp. 583–619.
- <sup>28</sup>Coder, J., and Maughmer, M. D., "Computational Fluid Dynamics Compatible Transition Modeling Using an Amplification Factor Transport Equation," *AIAA Journal*, vol. 52, 2014, pp. 2506–2512.
- <sup>29</sup>Coder, J., "Enhancement of the Amplification Factor Transport Transition Modeling Framework," 55th AIAA Aerospace Sciences Meeting, Grapevine, Texas, 2017.
- <sup>30</sup>Roget, B., Blumenstein, R., Saberi, H., and Sitaraman, J., "Advanced Rotorcraft Aeromechanics Simulations Using CREATE-AV Helios," Vertical Flight Society 75th Annual Forum & Technology Display, Philadelphia, Pennsylvania, May 13-16, 2019.